

A Multi-Bit Neuromorphic Weight Cell using Ferroelectric FETs, suitable for SoC Integration

Borna Obradovic, Titash Rakshit, Ryan Hatcher, Jorge Kittl, Rwik Sengupta, Joon Goo Hong, and Mark S. Rodder

Abstract—A multi-bit digital weight cell for high-performance, inference-only non-GPU-like neuromorphic accelerators is presented. The cell is designed with simplicity of peripheral circuitry in mind. Non-volatile storage of weights which eliminates the need for DRAM access is based on FeFETs and is purely digital. The Multiply-and-Accumulate operation is performed using passive resistors, gated by FeFETs. The resulting weight cell offers a high degree of linearity and a large ON/OFF ratio. The key performance tradeoffs are investigated, and the device requirements are elucidated.

Index Terms—Neuromorphic, FeFET, DNN

I. INTRODUCTION

HARDWARE accelerators for Deep Neural Nets (DNNs) are receiving increased attention as Neural Network-based applications proliferate. Currently, hardware accelerators fall into two categories: GPU-like devices [1] with reduced-precision arithmetic (and possibly an improved memory access architecture), and more “literal” implementations of DNNs as sets of resistive cross-bar arrays ([2], [3], [4], [5], [6]). While the former approach is already seeing practical use, the latter is still in the research phase. The key characteristics of the “literal” approach are local storage of network weights and analog computation of the outputs as linear combinations of inputs. By storing network weights locally, the time and energy required to copy them from off-chip DRAM is eliminated. The specific array architectures, weight cells, and even details of operation are still being investigated and vary considerably across implementations. One of the key design decisions is whether to support on-chip training ([1], [2], [5]), or whether weights are to be transferred to the chip after off-line training [7]. Each approach has advantages and disadvantages. On-chip training offers the most local customizability, as well as a near-complete suppression of the impact of process variability (since the training is done for the specific hardware). The key disadvantages are the significantly increased complexity of the peripheral circuitry needed to support on-chip backpropagation, as well as the much higher required precision of the weights (to handle the many small increments in the weights during the iterative training process). Implementations with off-chip training are more straightforward to program, but must contend with process variability impacting weight values and imperfect programming [7]. It should be noted that off-chip training with analog or multi-bit digital weights which are implemented as multiple states of a single device suffers from similar programming complexity as on-chip programming.

Due to the non-linearity of the response of all standard NVMs, the number or duration of programming pulses to achieve a desired weight depends on the current state of the weight ([2], [7]). A sense-program iteration is therefore required to achieve the desired weight, even though the value for the target weight was computed off-line.

In this paper, the assumption is made that near-term applications for neuromorphic accelerators on mobile SoCs will not benefit from on-chip training, which is instead relegated to the cloud. The focus is on improved inference performance and power reduction. The cross-bar array and non-volatile weight cells are designed for programming simplicity and robustness w.r.t. process and programming variability, enabling effective transfer of off-line weights. No iterative programming is required. Additionally, all training is assumed to be centralized (with possibly crowd-sourced data).

In order to achieve reasonable immunity to process variability and programming errors, a multi-bit digital representation of weights is used. It has been demonstrated (in this work and elsewhere) that high weight precision is not required for inference-only applications.

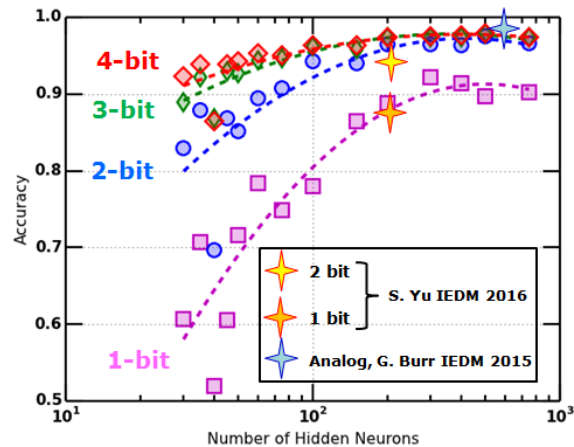


Fig. 1. The weight-precision/layer size tradeoff in DNN test accuracy is illustrated, using the MNIST benchmark. A single hidden layer of varying size is simulated with varying weight precision. The weights are obtained using standard training in software, then quantized for test accuracy evaluation. The quantization range is optimized separately for each point; results with the optimized quantization window are shown.

As seen in Fig. 1, even 2-bit weights achieve near-analog levels of accuracy with reasonably-sized, fully connected layers on a simple benchmark such as MNIST. Additionally, it is also possible to re-train a network to use larger layers if additional accuracy is required; choosing 2-bit weights therefore does not impose an overall inference accuracy constraint. Finally,

it should be noted that the results of Fig. 1 are obtained by straightforward quantization of software-trained network (with the additional step of optimizing the quantization window). If the network is trained with the assumption of quantized weights, even better accuracy can be obtained.

II. ARCHITECTURE

The array architecture is a slightly modified resistive cross-bar array, as shown in Fig. 2. The standard approach of using two weights to represent positive and negative conductances is used. The modification of the standard approach arises only in the use of dedicated program lines; one for each bit and for each row of weights. The program lines are shared across the entire row of weights; selecting individual weights to program is accomplished using the select lines. In inference mode, the program lines are grounded, and the weights behave like two-terminal devices, forming a cross-bar between the signal input and output lines.

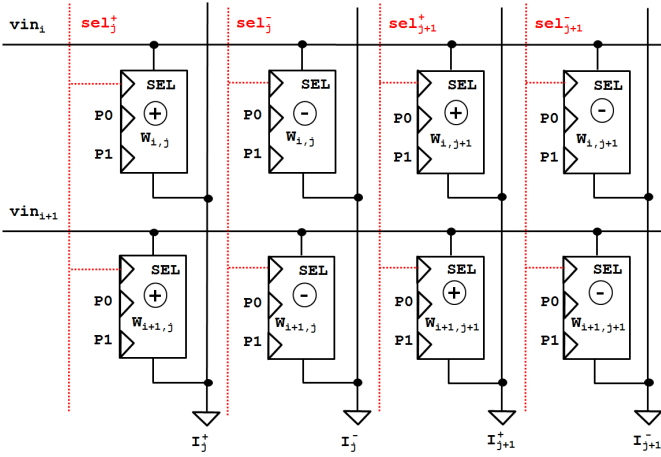


Fig. 2. The cross-bar array utilized in this work is illustrated. The array consists of two sets of weights: one each for positive and negative conductance contributions. An additional feature of the array is the set of dedicated program lines, used only during the programming events. Two-bit weights are shown, as indicated by the two programming inputs P0 and P1. Note that each sign contribution to the weight has two bits.

The resistive weight cells are composed of a parallel combination of passive resistors, with each passive resistor in series with a gating transistor (as illustrated in Fig. 3). The gating transistor could be a FeFET or a Flash transistor, or other FET-based NVM. In this work, we describe an architecture using a FeFET as the gating transistor, with the FeFET composed of a standard FET with a ferroelectric capacitor (FeCap) in the BEOL layers. The FeFET gate and BEOL physical structure is shown in Fig. 4. Electrically, this is similar to the integrated FeFET structure of [13].

The resistance values of the passive resistors for the weight cell are chosen as R_0 , $\frac{1}{2}R_0$, $\frac{1}{4}R_0$ etc. Conversely, the conductance of each branch (neglecting the influence of the transistors) is given by G_0 , $2G_0$, $4G_0$ etc. Denoting the logic state of each transistor (indexed by i) as b_i , the overall conductance of the cell is given as:

$$G_{tot} = G_0 \sum_{i=0}^{n-1} b_i 2^i \quad (1)$$

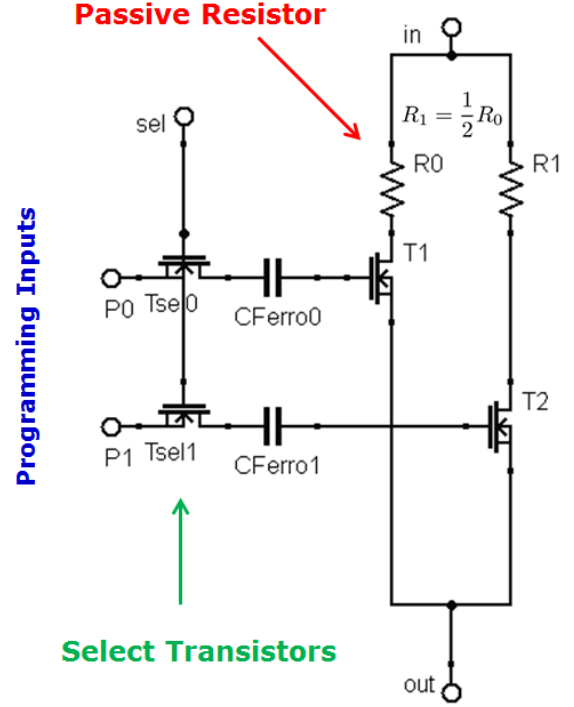


Fig. 3. The schematic of a two-bit weight cell is illustrated. The resistance is provided by passive resistors, while the NVM transistors enable or disable the individual branches. A select transistor is provided for each bit. Additional bits require additional parallel branches of resistor-transistor combinations. During inference, the program inputs are grounded and the weight cell acts as a two-terminal device. The values of the passive resistors are chosen to provide a binary ladder of overall weight conductance.

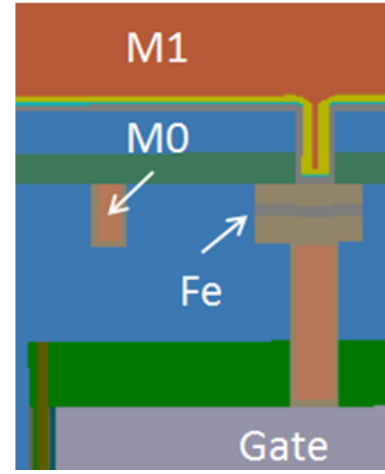


Fig. 4. The cross-section of an emulated FeFET structure is illustrated. The underlying FETs and gate are at the bottom, with the ferroelectric layer and surrounding metal electrodes placed at the M0 level.

where n is the number of bits in the cell ($n = 2$ in the example of Fig. 3). The state of the transistors is set by program and erase cycles (described in section IV), with the SEL input active. During inference, the program inputs (P_i) are grounded, and the potential on the gate of the transistors is determined by the polarization state of the ferroelectric capacitors. The programming is assumed to result in strongly-ON or strongly-OFF transistors (i.e. strongly negative or strongly positive

V_t , respectively), resulting in branch conductances that are (ideally) independent of the properties of the transistors or the precise programming of the FeCaps.

III. FERROELECTRIC CAPACITOR: PROPERTIES AND MODELING

The FeCaps shown in Fig. 3 are the enablers for the non-volatile operation of the weight cell. The desirable property of the FeCaps is the hysteretic behavior of the polarization, as illustrated in Fig. 5 (using measured data from [10]).

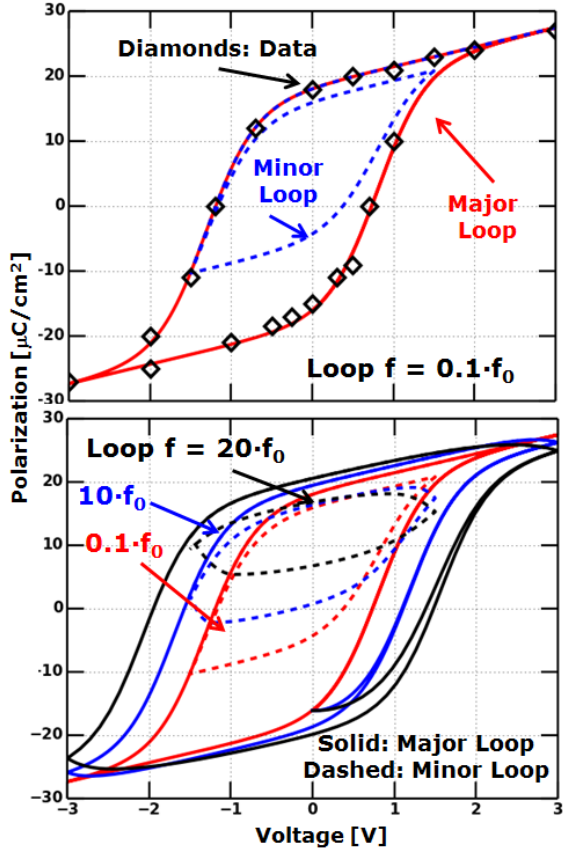


Fig. 5. The simulated polarization hysteresis of a HfZrO₂ FeCap is shown (measured data from [10]). The top figure illustrates the calibration to data on the outer (saturation) hysteresis loop, as well as the modeled behavior of an example minor loop (the minor loop is achieved by moving from positive saturation to a negative voltage equal to one-half of the max voltage, then swinging to a positive half-max voltage). The bottom figure illustrates the modeled frequency response. When the loop frequency is much longer than the ferroelectric domain response frequency f_0 , the behavior of the FeCap is quasistatic. For increased loop frequencies, the hysteresis loop becomes quite distorted, with an apparent increase in coercive voltage and a flattening of the minor loops.

In this work, the hysteretic behavior of FeCaps is modeled using a Preisach-based [9], turning-point model with explicit internal polarization dynamics. The quasi-static ferroelectric polarization is described next. The "raw" response function is given by:

$$F^\mp(V_{int}) = \theta^\pm \cdot \tanh\left(\frac{V_{int} \pm V_c^\pm}{V_{sc}^\pm}\right) \quad (2)$$

where V_{int} is the voltage representing the internal state of the FeCap (related to the applied voltage, as described next), V_c^\pm

and V_{sc}^\pm model parameters describing the coercive voltages and the voltage scales, respectively. Likewise, θ^\pm is a model parameter which sets the polarization strength in each state. Each quantity in Eqn. 2 has a "plus" and "minus" label, depending on whether the capacitor last experienced an increase or decrease in applied voltage (respectively). This is referred to as the "state" of the FeCap. The actual ferroelectric polarization P_{FE} is computed using Eqn. 3:

$$P_{FE}(V_{int}) = \left(F^\pm(V_{int}) - F_j^+\right) \cdot \left[\frac{P_j - P_i}{F_j^+ - F_i^-}\right] + P_j \quad (3)$$

where the indices i, j denote the currently active turning points, with $V_j > V_i$. Likewise, the quantities F_j^+, F_i^-, P_j , and P_i are evaluated at the current active pair of turning points. Eqn. 3 simply provides scaling and shifting of the raw response of Eqn. 2 to insure that the polarization curve passes through the active pair of turning points (this is necessary to provide reasonable minor-loop behavior). As is standard for turning-point models, turning points themselves are created and destroyed dynamically as the internal voltage of the FeCap switches. The ferroelectric response is thus modeled as a quasi-static function of the "internal" state of the FeCap (described by V_{int}). The overall behavior of the FeCap is therefore dependent on the dynamics of V_{int} . In this work, V_{int} is governed by a second-order delay of the applied voltage across the FeCap. Specifically, the differential equation relating the "internal" voltage V_{int} and the applied voltage V_{app} is given as:

$$\ddot{V}_{int} + 2\gamma\omega_0\dot{V}_{int} + \omega_0^2V_{int} = \omega_0^2V_{app} \quad (4)$$

where the natural frequency ω_0 and the damping ratio γ are calibration parameters of the model. The "memory" property of the FeCap is handled by the model through the turning point history and the active state. Both are changed in a discrete manner, when the temporal derivative of V_{int} changes sign. This ensures that the state itself is not experiencing the second-order dynamics described in Eqn. 4; the dynamics merely provide a delay for an abrupt switching of the state. It should be noted that the second-order delay model of Eqn. 4 is purely empirical. It is merely used in this work to provide a delayed response for the switching of ferroelectric domains. No attempt is made to provide a detailed frequency-dependence calibration to a specific material. It has been shown in the literature that the frequency response of ferroelectric materials covers a very wide range; from a very fast responses in the 10s of ns [11], to a much slower 10s of μ s [12]. For the purposes of this work, it is assumed that the ferroelectric material has a switching frequency comparable to the fast material of [11]. For materials where this is not the case, the programming times discussed in IV must be adjusted to accommodate the slower frequency response. Finally, the total charge of the capacitor is computed as:

$$Q_{tot}(V_{int}, V_{app}) = (P(V_{int}) + C_{lin}V_{app}) \cdot A \quad (5)$$

where C_{lin} is the non-ferroelectric capacitance, and A is the total capacitor area. The non-ferroelectric response is modeled

as being driven by the instantaneous applied voltage V_{app} , since the non-ferroelectric response is assumed to be much faster than any modulation of the applied voltage. For the purpose of this work, the complete model is implemented in Verilog-A and used within Synopsys HSPICE.

IV. PROGRAM AND ERASE

In order to assign the weights of the neural network, the FeCaps must be programmed to appropriate states. This can be performed by applying voltage pulses to either the program terminals or the in/out terminals of the weight. Program and erase schemes for the FeCaps are illustrated in Fig. 6. In this work, a programming scheme which results in a positive after-pulse voltage on the gate node of the underlying FET is termed "Program," whereas a scheme which results in a negative after-pulse gate voltage is termed "Erase." In the example array of Fig. 2, a select transistor is needed in order to enable programming, since only a single set of program interconnect lines can be provided for each row of the crossbar array. Since the weights of a given row share program lines, the column which is being programmed at any given time is selected by activating the appropriate select line.

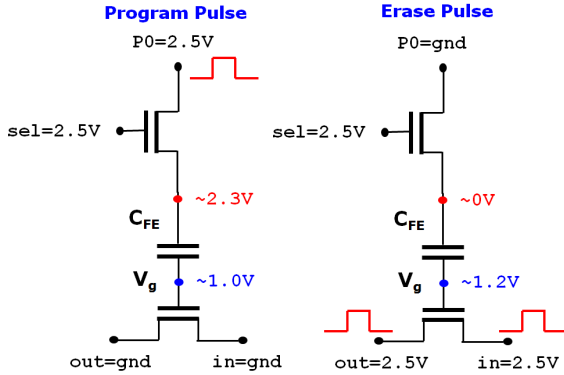


Fig. 6. The "Program" and "Erase" schemes for the FeCaps are illustrated. In both cases, a suitably large voltage is established across the FeCap, with opposite polarities in the two conditions. Due to capacitive voltage division across the FeCap and the FET (and to a lesser extent the select transistor as well), the voltage across the FeCap is considerably smaller than that of the applied pulse. Given the relatively large coercive voltages available in current technologies, the programming is necessarily done at moderately high voltages.

An additional constraint is the fact that the individual FeFETs of a given weight share common in/out terminals. It is therefore not possible to erase them individually, using the scheme of Fig. 6. One possible programming strategy is therefore to initially fully erase an array, with all FeCaps set to the erased state, followed by individual programming of FeCaps which need to be in the programmed states. This is somewhat akin to "flash" erase commonly used for various Flash technologies. Both erase and program are expected to take place infrequently: only when the neural network is initially mapped onto the SoC. During inference operations (which are expected to be frequent), no erase or program operations take place. Figures 7 (top and bottom, respectively) illustrate program and erase events in more detail. In Fig. 7(top) a single bit is cycled several times by alternating erase

and program pulses and ultimately left in a programmed state. The cycling is performed to ensure that the state of the bit is independent of the initial condition. The P-V trajectory for the erase-program cycle is illustrated in Fig. 8. Simulation begins with zero charge on the FeCap, in state 1. After the initial erase (arc 2), the first program pulse takes the FeCap to the highest achievable positive voltage, along arcs 3 and 4 of Fig. 8. This corresponds to the peak voltage point under the program pulse in Fig. 7. After the programming pulse ends (as V_{app} is reduced to zero), the FeCap P-V trajectory continues along the steady-state loop (Fig. 8) until it intersects the FET C_{gg} load-line (the FET is now in strong inversion and has a nearly constant capacitance). The FET C_{gg} load line is simply established from the equation for the voltage drop across the FeFET stack:

$$V_{app} = V_{cap} + V_g \quad (6)$$

After the program pulse is completed, Eqn. 6 reads simply $V_{cap} = -V_g$, and with the condition that $Q_{cap} = Q_g$, the loadline can be established as

$$P_{cap} \approx -\frac{C_{gg}}{A_{cap}} \cdot V_{cap} \quad (7)$$

The equation for the loadline is approximate, since the FET gate capacitance is not constant. The final voltage across the FeCap after a programming even is negative (approximately $-0.5V$). Correspondingly, the voltage on the gate node of the FET is approximately positive $0.5V$, putting the FET into a (relatively) weak ON-state. This is the "Programmed" condition. The application of the erase pulse (achieved by simultaneously pulsing the in/out terminals while grounding the program terminal) makes the FeCap voltage more negative, continuing the P-V trajectory from the program point, all the way to the most negative voltage on the steady-state loop. After the erase pulse is completed, the P-V trajectory continues until it intersects the FET C_g load-line at a slightly positive voltage. The slightly positive voltage of the FeCap with a grounded program line implies a slightly negative voltage on the gate of the FET (simulations indicate approximately $-0.25V$). Given that a typical V_t of the FET is approximately 350 mV, the erase cycle has left it in a strongly OFF condition. This is the "Erased" condition.

While Fig. 7(top) left the FeCap in a programmed state, Fig. 7(bottom) illustrates how the erase (or rather, the "non-program") is accomplished instead. Since all FeCaps are initially erased, the select transistor is used to make sure that program events don't change the state of FeCaps which must remain erased. The **sel** input is set to **gnd** during the last program pulse of 7, preventing programming from taking place. The final voltage on the gate of the FET is equal to that of the initial erased state. It should be noted from Fig. 8 that due to voltage division between the FeCap and the FET, the FeCaps in this example operate on a minor loop which is much smaller than the outer saturation loop. This indicates that much stronger programming is theoretically possible. In order to reach the saturation loop and correspondingly stronger ON-states of the FET, significantly higher programming voltages are required. Furthermore, the use of an nFET for the select device implies that the highest voltage across the FeFET is

the lesser of $V_{select} - V_t$ and $V_{program}$. High programming voltages therefore imply high V_{gs} values for the select device, suggesting that a high voltage design is required.

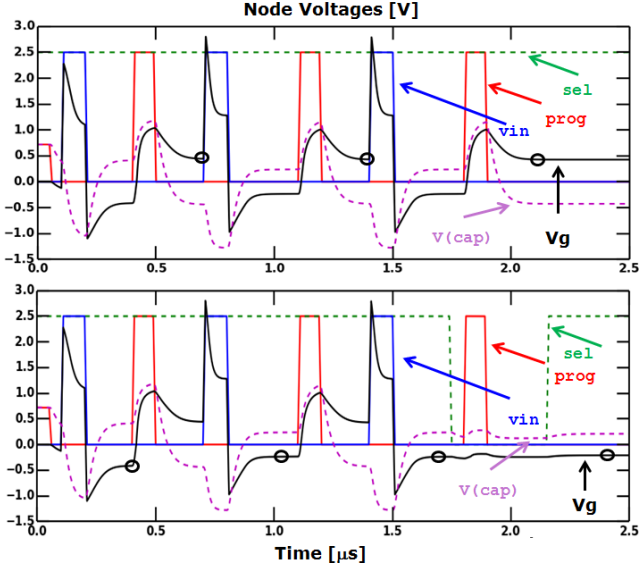


Fig. 7. The simulated cycle of erase and program events for a single bit. After the initial erase and program event, the nodal voltages exhibit steady-state behavior. The final voltage on the gate of the FET indicates the programming strength of the bit. The program event is shown in the top figure, the erase event is shown in the bottom figure. The non-quasistatic behavior is almost entirely due to the delaying dynamics of the FeCap; the RC time constants are much shorter than the clock period.

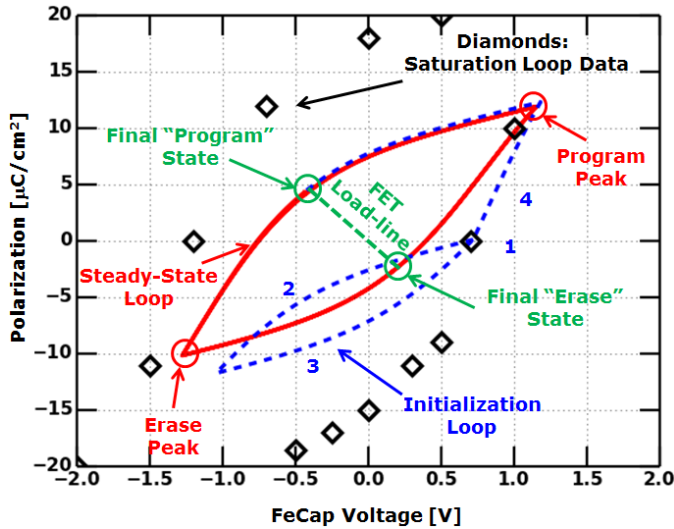


Fig. 8. The simulated polarization hysteresis of a set of program and erase cycles is shown. The initialization loop is shown as a blue dashed line, while the steady-state loop is indicated with a solid red line. The saturation loop data (to which the model is calibrated) is shown with black symbols. Note that the steady-state loop is much smaller than the saturation loop.

In this work, since the FeCaps are implemented in the BEOL levels, the area of the FeCaps is tunable and there is no layout area penalty associated with FeCap size. It is therefore possible to choose the FeCap area which maximizes the $\Delta V_{prog} = V_{prog} - V_{erase}$ voltage window. The behavior of the program and erase loop as a function of FeCap area

is illustrated in Fig. 9. Increasing the FeCap area results in a smaller voltage drop across the FeCap during programming. This constricts the size of the minor loop for the program/erase cycle, with lower end voltages and lower polarizations. This is seen in Fig. 9 as a tightening of the polarization loop with increasing area. At the same time, the increased area increases the total charge, resulting in higher peak charge values on the FeCap and FET gate (in spite of the reduced charge/unit area). This is reflected in Fig. 9 as higher peak charge values at the ends of the polarization loops. The final program and erase voltages are obtained from the intersection of each polarization loop with the zero- V_{app} C_{gg} load line of the FET.

It can be seen that the locus of the intersection varies non-monotonically with FeCap area (especially for the program portion of the loop), due to the competing effects of reducing polarization and increasing area. The maximum in the $\Delta V_{prog} = V_{prog} - V_{erase}$ voltage window is obtained for an FeCap area of 1250 nm^2 (given the particulars of the underlying FETs and the FeCap hysteresis curve). Significantly larger or smaller areas result in degraded programming performance.

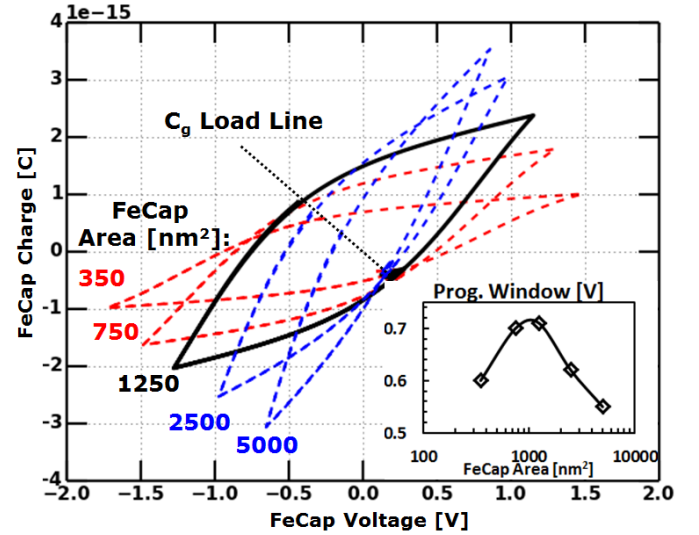


Fig. 9. The effect of FeCap area on the program and erase conditions is illustrated. The behavior of ΔV_{prog} is clearly non-monotonic w.r.t. FeCap area. Very small FeCaps have large peak programming voltages, but reduced ΔV_{prog} due to an overall reduction in charge (small area). Very large FeCaps have small programming voltages since most of the applied voltage is dropped across the FET gate, and likewise result in reduced ΔV_{prog} .

V. PASSIVE RESISTOR

An important element of the multi-bit weight cell of Fig. 3 is the passive resistor. The resistance value of the resistor could be chosen so that when the FeFET in a branch of the cell is in the ON-state, the resistance of the passive resistor is much larger than that of the FET. If this is the case, then the non-linear behavior of the FET will have a negligible effect on the overall conductance of the cell. Given that the resistance of the FET is expected to be in the range of a few $k\Omega$, the passive resistor should have a resistance in the range of $30k\Omega$ to $100k\Omega$. Larger values of resistance result in better overall linearity, but also limit the current. With the stated

resistance range, currents supplying the summing amplifiers are in the reasonable range of a few to a few tens of μA . There are many options for implementing the passive resistor, with varying tradeoffs on size, variability and linearity. One possible approach is to simply use the channel of a FET as the body of the passive resistor.

Simulations of such resistors (Fig. 10) indicate that the desired resistance level can be achieved with reasonably good linearity.

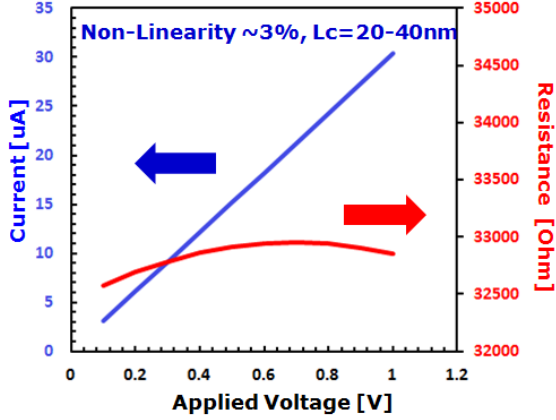


Fig. 10. The resistor current and resistance values are shown. The target resistance values of a few tens of $k\Omega$ appear to be achievable, and the value of the resistance is very nearly constant over a wide range of applied voltages.

A concern with doped resistors is the RDF-induced variability. Unlike a FET with a doped channel, the question is not one of V_t -variability, but simply that of variable "bulk" conductance due to the random number of dopants in any one resistor. As such, the variability of conductance (assuming Poisson-distributed number of dopants per channel) can be expressed as:

$$\frac{\sigma(G)}{G} = \frac{1}{\sqrt{N}} \quad (8)$$

where G is the conductance of the resistor body, $\sigma(G)$ is the RDF-induced standard deviation of the conductance, and N is the total (expected) number of atoms in the resistor body. Given reasonable resistor dimensions, lengths, and target doping values, the expected number of atoms is ~ 100 , resulting in a relative standard deviation of $\sim 10\%$. While this may seem like a large uncertainty in the conductance (and therefore in the neural net weight), it is of relatively little consequence in typical fully-connected layers. This is illustrated in Fig. 11, where the accuracy of a neural net is evaluated with various levels of uncorrelated noise.

A single hidden-layer network with various sizes of the hidden layer is trained for MNIST. The weights are quantized to two-bit precision and perturbed using a Poisson distribution, as indicated by Eqn. 8. A set of MC simulations is then performed with various levels of perturbation. As can be seen from Fig. 11, there is no significant loss of classification accuracy until the relative weight perturbation is on the order of 30%. This is not surprising for fully-connected architectures, such as the one used. The large number of inputs to any one neuron induce partial noise cancellation, with the expected standard deviation

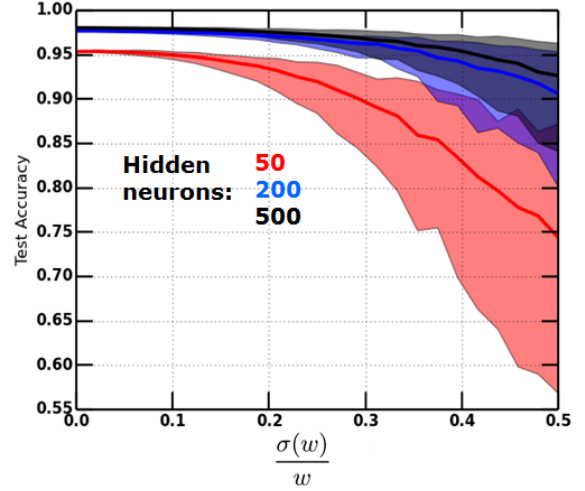


Fig. 11. The effect of uncorrelated resistor noise due to RDF-induced variability is evaluated by simulation. The expected regime of noise for the passive resistors described in this work is $< 10\%$. With reasonable hidden-layer sizes, the effect of this level of noise is negligible.

of the total input to the neuron scaling by $1/\sqrt{N_{inp}}$, N_{inp} being the number of inputs. The larger the network layers then, the less susceptibility to uncorrelated weight noise there is. Given the expected level of $< 10\%$, the RDF of the resistors appears to be satisfactory.

VI. TRANSISTOR

An important parameter of the underlying FET of the FeFET structure is the threshold voltage. There are typically two or three V_t levels provided, but the FeFET requirements place restrictions on the choice. This is illustrated in Fig. 12.

As seen in Fig. 12, the application of the input voltage to the weight cell causes a slight shift in the V_g node voltage. This is a result of the capacitive coupling of the FET drain and gate, both due to the parasitic and intrinsic coupled charge. The effect is particularly pronounced on erased bits, since very little current flows in the erased branch, and essentially the entire input voltage is applied to the drain of the FET. The IR drop across the resistor lessens the impact in branches with programmed bits. Fig. 12 illustrates a possible band of V_t values for the FET. For all applied input voltages, the erased transistor has a gate voltage significantly below the FET V_t . This ensures that the erased transistor remains turned off (the extent to which it is turned off is a technology parameter that sets the max ON/OFF ratio of the weights). The V_t is also low enough so that the programmed transistor has sufficient gate overdrive to keep the transistor conductance much higher than that of the passive resistor. Thus, the choice of the V_t falls into a somewhat narrow band, and induces a tradeoff between weight accuracy and linearity on one hand (V_t must be low), and low conductance of the zero weights (V_t must be high). V_t values in the 200-300 mV range needed for the implementation shown in this paper are typically readily available in modern CMOS technologies.

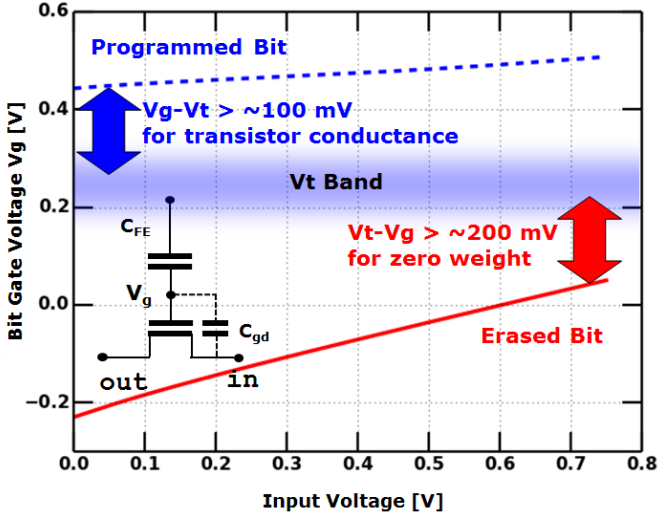


Fig. 12. The allowed V_t -band of the underlying FETs is illustrated, along with the behavior of V_g with applied input voltage. The V_t must be low enough so that the programmed V_g exceeds it by at least 100 mV, enabling sufficient gate overdrive to keep the conductance of the transistor much higher than that of the passive resistor. Likewise, the V_t must also be high enough so that the V_g of the erased bits is always at least approximately 200 mV below it to make sure that the FET never turns on significantly. Satisfying both criteria simultaneously results in a narrow band of allowable V_t values. The V_g of the FET varies with the applied input voltage due to capacitive coupling of the drain and gate (both parasitic and intrinsic).

VII. RESULTS

Having programmed the individual FeFETs in the array, inference can be performed simply by applying input voltages (fixed levels or pulses) to the array. The program lines are all grounded during inference. In this mode, each weigh cell acts as a two-terminal device. For the case of the two-bit cell, the I-V characteristics are illustrated in Fig. 13.

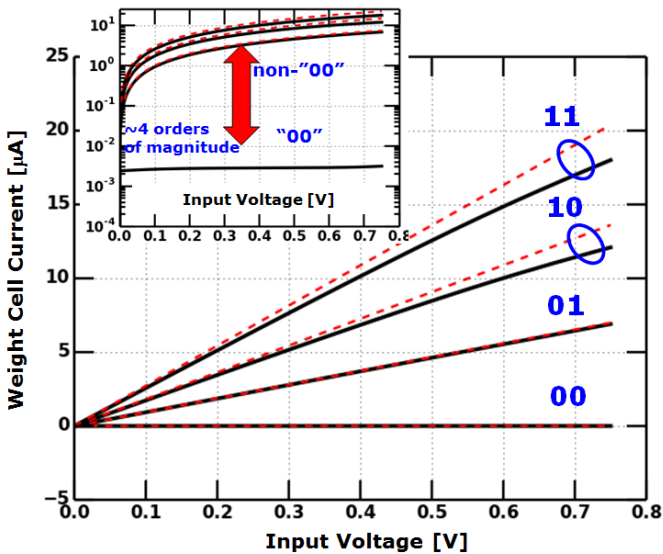


Fig. 13. The I-V relationship for a two-bit weight cell is illustrated for all four programming combinations. The simulated current is shown in black, while the ideal currents (as if the weight cells were ideal resistors) are shown as dashed red lines. The inset shows the same currents on a logarithmic scale, illustrating the large dynamic range of currents available.

The I-V characteristics of Fig. 13 show good linearity over a wide range of input voltages, with appreciable deviation seen only for the highest current conditions. The dynamic range of ON/OFF currents is roughly four orders of magnitude, considerably larger than for memristive devices. This makes the multi-bit weight cell suitable for arrays with large numbers of inputs. The accuracy of the various ON-states is further illustrated in Fig. 14.

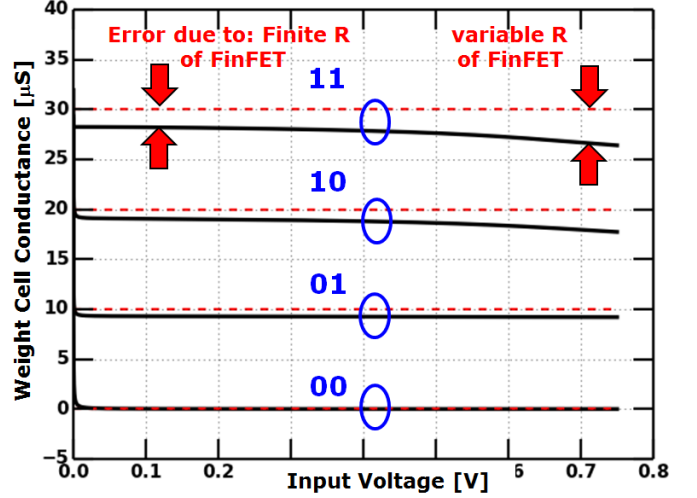


Fig. 14. The conductances of the four states of the two-bit weight cell are shown. Solid black lines are simulated conductances, dashed red lines represent ideal values. The error at low input voltage is attributable to the finite resistance of the FET in linear mode. At high voltages, the error increases due to the larger FET resistance in saturation.

It is evident from Fig. 14 that the absolute accuracy of the weights is quite good when the weights are small, but the weights become increasingly less accurate as the nominal weight value increases. This is simply a result of the finite (and non-linear) resistance of the FET increasing the total series resistance. The effect is negligible for the small weights since the resistance of the passive resistor in those cases is large. Similarly, the accuracy is best for small values of the input signal but shows increasing error with the signal voltage. This is due to the transition of the FET from the linear to the saturation regime as the V_{ds} across the FET increases (particularly sensitive for large weight branches where the resistance of the passive resistor is small). Given the expected deviations of the hardware weights from ideality, it is necessary to simulate the accuracy of the overall neural net. The standard simple MNIST benchmark is used, as shown in Fig. 15. In addition to the quantized weights as described in this work, the neuronal activations are considered to be binarized. While this is certainly not necessary, binarization greatly simplifies the problem of transferring signals from one layer to the next, eliminating the need for ADC/DAC conversion.

As can be seen in Fig. 15, the networks with non-ideal weights and binarized activations do indeed suffer some accuracy loss, as compared to ideal multi-bit weights (Fig. 1). The degree of accuracy loss depends on the regularization procedure, however. Points in Fig. 15 are obtained by direct quantization of weights from software-based training. Dashed

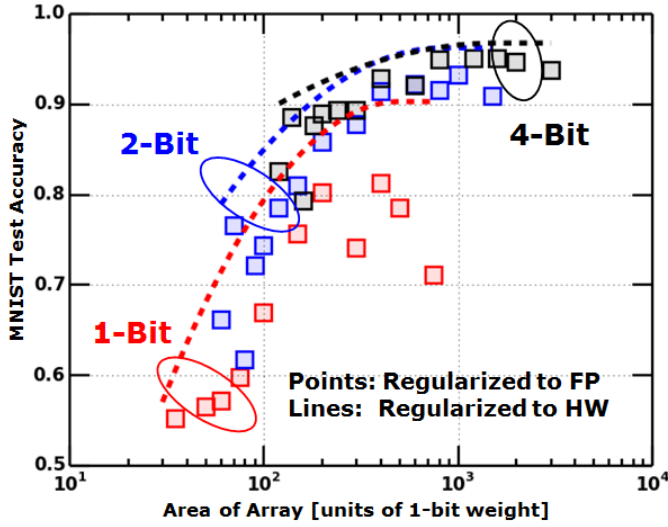


Fig. 15. The test accuracy on the MNIST benchmark is computed with weight models describing the FeFET-based weight cells. Weights are quantized to 1, 2, and 4-bit precision. The quantized weights are non-linear as described by Fig. 14. All activations are binarized. The accuracy is plotted vs. the total array area (number of cells times the cell area).

lines are obtained using weights which were trained using hardware-aware regularization. While both sets of data use regularization, the inference on the validation set for the second group was performed using the full hardware model, including weight quantization, weight non-idealities, and binarization of activations. The algorithm is summarized in Alg. 1. The validation accuracy thus obtained is a much better estimate of the final test accuracy (which also uses non-ideal weights and activations), yielding much better test accuracies overall. This is particularly evident in cases where the neural network is over-provisioned (large arrays), and significant over-fitting occurs if the network is not properly regularized. With hardware-aware regularization, it can be seen that the test accuracy does not degrade for large arrays, and test accuracies are significantly better overall. Even better results should be obtainable if the training procedure itself is hardware-aware [14].

Algorithm 1: Hardware-Aware L^2 Regularization

```

1 Regularization Algorithm ( $train, validate, \lambda$ );
   Input : Training set  $train$ , validation set  $validate$ ,
            $\lambda_{min}, \lambda_{max}$ 
   Output:  $w_{optim}$ 
2 for  $\lambda_i = \lambda_{min}$  to  $\lambda_{max}$  do
3   Set  $w_i = Train(\lambda_i, train)$ 
4   for  $qw_j = qw_{min}$  to  $qw_{max}$  do
5     Set  $w_{ij}^{HW} = HWModel(w_i, qw_j, validate)$ 
6   end
7   Set  $cost_{ij} = Validate(w_{ij}^{HW})$ 
8 end
9 return  $w^{HW}(argmin(cost_{ij}))$ 

```

VIII. SUMMARY AND CONCLUSION

A multi-bit weight cell for analog MAC in neuromorphic arrays was presented. The cell supports in-memory computing based on NVM-storage of weights, removing the need for DRAM access during inference (unlike GPU-like implementations such as [1]). It was shown that for inference purposes, a small number of bits are sufficient for analog-like accuracy. The proposed multi-bit weight cell uses an FeFET as gating element in each branch of a circuit consisting of a parallel combination branches of passive resistors. The resistor weights are arranged in a binary ladder, enabling a uniform distribution of conductances to be programmed into the cell. The FeFETs are constructed using standard FETs as the underlying FET element, with FeCaps in the BEOL connected to FET gates. The polarization state of the FeCaps stores the individual bits of the weight. It was suggested that passive resistors can be formed using FETs. The program and erase cycles for the cell were described, and it was found that moderately high voltages are needed for acceptable programming levels. It was found that up to 700 mV of differential programming (difference in FET V_t between programmed and erased states) could be achieved using standard CMOS processes and literature-based FeCap properties. With this level of programming, an acceptable level of weight linearity could be achieved, along with an ON/OFF ratio for the weights in excess of four orders of magnitude. Finally, it was shown that even with the non-ideal weights formed by the multi-bit circuits, a high level of inference accuracy is possible (using the MNIST benchmark). This is particularly true if the regularization is hardware-aware, i.e. cross-validation is performed using the actual weight model, with an optimized quantization window. Failure to do so results in somewhat sub-optimal weight transfer from software to hardware, and an associated degradation in test accuracy. It was also noted that the area efficiency of the cell is independent of the number of bits used (except for the 1-bit case); at matched array area, the 2-bit and 4-bit cells produced the same level of inference accuracy. An unrecoverable loss was only observed with 1-bit cells. Further improvements in weight ideality require improved FeCap properties. Increased ferroelectric polarization (relative to the non-ferroelectric polarization) would result in increased V_t differentials between the programmed and erased states, enabling better linearity and further improved ON/OFF ratio.

REFERENCES

- [1] N.P. Jouppi, et al., "In-Datacenter Performance Analysis of a Tensor Processing Unit", arXiv:1704.04760
- [2] Z. Li, P.Y. Chen, H. Xu, S. Yu, "Design of Ternary Neural Network With 3-D Vertical RRAM Array *IEEE Transactions on Electron Devices* 64 (6), 2721-2727
- [3] P. Yao, H. Wu, B. Gao, N. Deng, S. Yu, H. Qian, "Online training on RRAM based neuromorphic network: Experimental demonstration and operation scheme optimization", Jun 13 2017 2017 IEEE Electron Devices Technology and Manufacturing Conference, EDTM 2017 - Proceedings. Institute of Electrical and Electronics Engineers Inc., p. 182-183 2 p. 7947592
- [4] S.B. Eryilmaz, D. Kuzum, S. Yu, H.S.P. Wong, "Device and system level design considerations for analog-non-volatile-memory based neuromorphic architectures", Feb 16 2016 Technical Digest - International Electron Devices Meeting, IEDM. Institute of Electrical and Electronics Engineers Inc., Vol. 2016-February, p. 4.1.1-4.1.4 7409622

- [5] S. Kim, M. Ishii, S. Lewis, T. Perri, M. BrightSky, W. Kim, R. Jordan, G.W. Burr, N. Sosa, A. Ray, J-P Han, C. Miller, K. Hosokawa, C. Lam, "NVM neuromorphic core with 64k-cell (256-by-256) phase change memory synaptic array with on-chip neuron circuits for continuous in-situ learning" IEEE International Electron Devices Meeting (IEDM) 2015
- [6] G.W. Burr, R.M. Shelby, A. Sebastian, S. Kim, S. Kim, S. Sidler, K. Virwani, M. Ishii, P. Narayanan, A. Fumarola, L.L. Sanches, I. Boybat, M.L. Gallo, K. Moon, J. Woo, H. Hwang, Y. Leblebicim, "Neuromorphic computing using non-volatile memory" Pages 89-124 — Received 31 Aug 2016, Accepted 01 Nov 2016, Published online: 04 Dec 2016
- [7] F.M. Bayat, X. Guo, M. Klachko, N. Do, K. Likharev, D. Strukov, "Model-based high-precision tuning of NOR flash memory cells for analog computing applications", Proceedings of DRC16, Newark, DE, June 2016
- [8] S. George, K. Ma, A. Aziz, X. Li, A. Khan, S. Salahuddin, M.F. Chang, S. Datta, J. Sampson, S. Gupta, V. Narayanan, "Nonvolatile Memory Design Based on Ferroelectric FETs", IEEE International Electron Devices Meeting (IEDM), 2016
- [9] G. Robert, D. Damjanovic, N. Setter "Preisach modeling of ferroelectric pinched loops" Appl. Phys. Lett. 77, 4413 (2000)
- [10] J. Muller, T.S. Boscke, D. Brauhaus, U. Schroder, U. Bottger, J. Sundqvist, P. Kcher, T. Mikolajick, L. Frey "Ferroelectric Zr_{0.5}Hf_{0.5}O₂ thin films for nonvolatile memory applications", Appl. Phys. Lett. 99, 112901 (2011)
- [11] J. Li, B. Nagaraj, H. Liang, W. Cao, C. H. Lee, R. Ramesh, "Ultrafast polarization switching in thin-film ferroelectrics" Appl. Phys. Lett. 84, 1174 (2004)
- [12] "Experimental Study on Polarization-Limited Operation Speed of Negative Capacitance FET with Ferroelectric HfO₂", M. Kobayashi, N. Ueyama, K. Jang, T. Hiramoto, IEEE International Electron Devices Meeting (IEDM), 2016
- [13] S. George, K. Ma, A. Aziz, X. Li, A. Khan, S. Salahuddin, M.F. Chang, S. Datta, J. Sampson, S. Gupta, V. Narayanan, "Nonvolatile Memory Design Based on Ferroelectric FETs", IEEE International Electron Devices Meeting (IEDM), 2016
- [14] M. Rastegari, V. Ordonez, J. Redmon, A. Farhadi "XNOR-Net: ImageNet Classification Using Binary Convolutional Neural Networks", arXiv:1603.05279